



# Impact of the spatial resolution on the energy balance components on an open-canopy olive orchard

J.M. Ramírez-Cuesta<sup>a,b,\*</sup>, R.G. Allen<sup>c</sup>, P.J. Zarco-Tejada<sup>d</sup>, A. Kilic<sup>e</sup>, C. Santos<sup>b</sup>, I.J. Lorite<sup>b</sup>

<sup>a</sup> Centro de Edafología y Biología Aplicada del Segura (CEBAS), Consejo Superior de Investigaciones Científicas (CSIC), Campus Universitario de Espinardo, 30100, Murcia, Spain

<sup>b</sup> IFAPA, Centro “Alameda del Obispo”, Avda. Menéndez Pidal s/n. 14004, Córdoba, Spain

<sup>c</sup> Kimberly Research Center, University of Idaho, Kimberly, ID, USA

<sup>d</sup> Instituto de Agricultura Sostenible (IAS), Consejo Superior de Investigaciones Científicas (CSIC), Avda. Menéndez Pidal s/n., 14004, Córdoba, Spain

<sup>e</sup> Department of Civil Engineering School of Natural Resources, University of Nebraska-Lincoln, Lincoln, NE, USA

## ARTICLE INFO

### Keywords:

Energy balance  
Spatial resolution  
Evapotranspiration  
METRIC model

## ABSTRACT

The recent technical improvements in the sensors used to acquire images from land surfaces has made possible to assess the performance of the energy balance models using unprecedented spatial resolutions. Thus, the objective of this work is to evaluate the response of the different energy balance components obtained from METRIC model as a function of the input pixel size. Very high spatial resolution airborne images ( $\approx 50$  cm) on three dates over olive orchards were used to aggregate different spatial resolutions, ranging from 5 m to 1 km. This study represents the first time that METRIC model has been run with such high spatial resolution imagery in heterogeneous agricultural systems, evaluating the effects caused by its aggregation into coarser pixel sizes. Net radiation and soil heat flux showed a near insensitive behavior to spatial resolution changes, reflecting that the emissivity and albedo respond linearly to pixel aggregation. However, greater discrepancies were obtained for sensible (up to 17%) and latent (up to 23%) heat fluxes at spatial resolutions coarser than  $30 \times 30$  m due to the aggregation of non-linear components, and to the inclusion of non-agricultural areas in such aggregation. Results obtained confirm the good performance of METRIC model when used with high spatial resolution imagery, whereas they warn of some major errors in crop evapotranspiration estimation when medium or large scales are used.

## 1. Introduction

An accurate assessment of irrigation requirements results crucial to improve water productivity, especially where water scarcity prevails (Allen et al., 1998; Pereira et al., 2002; Lovarelli et al., 2016; Winter et al., 2017). These irrigation requirements must counteract water losses due to evapotranspiration (ET), which includes plant transpiration and soil evaporation. The evapotranspiration process is dependent on meteorological variables (air temperature, relative humidity, solar radiation and wind speed), and crop parameters (vegetation status, height and density, vegetation fraction cover ( $F_c$ ), etc.) (Brutsaert, 1982).

The large number of factors controlling crop evapotranspiration ( $ET_c$ ), along with their interactions, make  $ET_c$  estimation a complex procedure. However, numerous methods are intended to estimate  $ET_c$ , differing between those based on field methods (soil water balance,

eddy covariance (EC), lysimeters, Bowen ratio, surface renewal, scintillometry, sap flow...) and those based on remote sensing, RS, techniques (surface energy balance, SEB, models; and vegetation index, VI, based models).

Field methods provide valuable continuous and nearly fully automated ET estimates. They are nondestructive methods that can measure ET over both reference ( $ET_o$ ) and non-reference ( $ET_c$ ) surfaces (Allen et al., 2011). Nevertheless, these methods based on field sensors show some drawbacks. Most of them require fragile and expensive equipment, and with some methodologies such as EC, a sizable fetch (and then, large field size) to achieve an equilibrium boundary layer deeper than the instrument installation height (Rana and Katerji, 2000; Allen et al., 2011; Kool et al., 2014). Additionally, field methods provide discrete measurements that may not be representative of the surrounding area (Idso et al., 1975a; Moran et al., 1989; Rana and Katerji, 2000; Allen et al., 2011). Thus, especially for measurements carried out

\* Corresponding author at: Centro de Edafología y Biología Aplicada del Segura (CEBAS), Consejo Superior de Investigaciones Científicas (CSIC), Campus Universitario de Espinardo, 30100, Murcia, Spain.

E-mail address: [ramirezcuesta.jm@gmail.com](mailto:ramirezcuesta.jm@gmail.com) (J.M. Ramírez-Cuesta).

<https://doi.org/10.1016/j.jag.2018.09.001>

Received 5 July 2018; Received in revised form 2 September 2018; Accepted 3 September 2018

0303-2434/ © 2018 Elsevier B.V. All rights reserved.

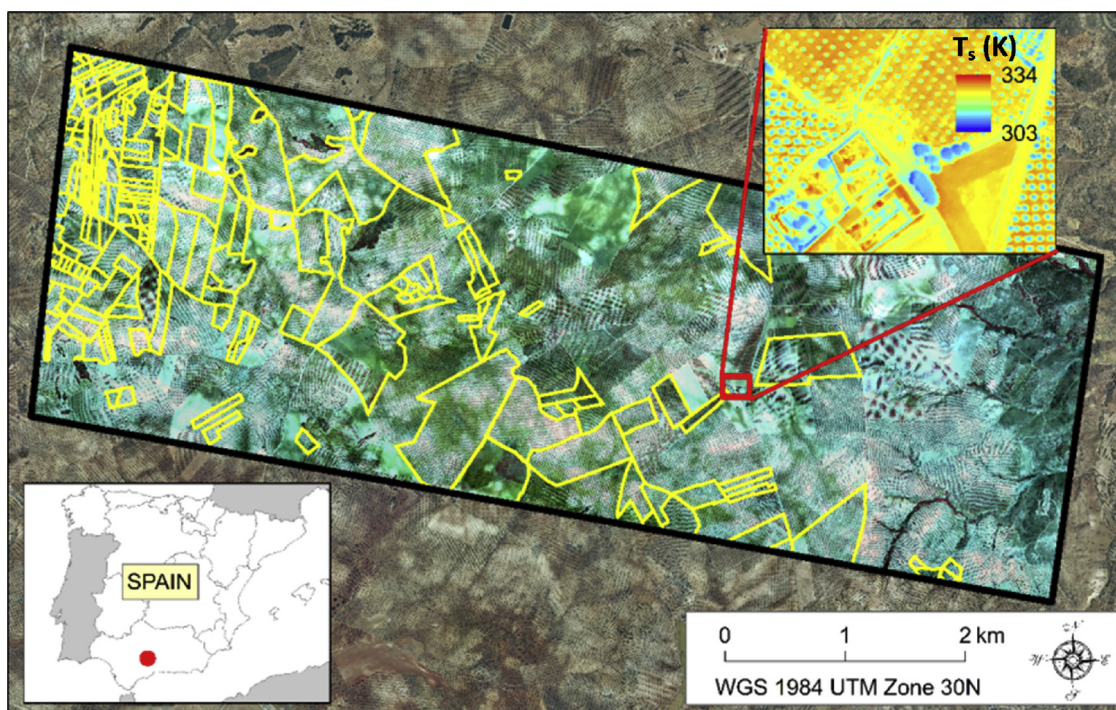


**Fig. 1.** False color composition (NIR-Red-Green) of the study area. Solid black line includes the area covered by the flights. The small rectangle in the upper-right corner shows an example of the thermal image. The fields considered in the analysis are represented by solid yellow lines. (For interpretation of the references to colour in this figure legend, the reader is referred to the web version of this article).

in orchards, heterogeneity hinders the characterization of field water-related properties, requiring dense sensors networks.

Techniques based on RS are generally more economic than field sensors measurements. Actual ET estimations of large areas may be provided by RS, allowing the assessment of the spatial ET variability (Norman et al., 1995; Bastiaanssen et al., 1998a; Allen et al., 2001; Su, 2002; Anderson et al., 2003; Allen et al., 2007a). The spatial resolution of these techniques varies according to the selected sensor, ranging from kilometers (e.g. MODIS, MVIRI, SEVIRI, GERB) to a few centimeters (e.g. sensors on-board Quickbird, Ikonos or aircrafts). Despite the advantages of RS techniques, these have similar limitations than field methods for orchard characterization and in fields with limited size. Thus, although the spatial resolution from satellites in the visible and near infrared (VNIR) has improved significantly in the last years, the thermal domain remains at the same (or even lower) spatial resolution than the one provided by the satellites in the early eighties. Furthermore, the physical processes within crop orchards, as the energy or water balance in the soil, become more complicated than in homogeneous crops due mainly to the structural complexity inherent in such heterogeneity.

The consideration of the previously described satellites such as Landsat or TERRA providing medium-high spatial resolution data, has allowed developing and validating models for ET assessment. These models include Surface Energy Balance Algorithm for Land, SEBAL (Bastiaanssen et al., 1998a, b); Mapping Evapotranspiration at High Resolution using Internalized Calibration, METRIC (Allen et al., 2007a, b); Surface Energy Balance System, SEBS (Su, 2002); SIMDualKc model (Rosa et al., 2012); Simplified Surface Energy Balance Index, S-SEBI (Roerink et al., 2000); operational Simplified Surface Energy Balance model, SSEBop (Senay et al., 2013), among others. However, it may be necessary to evaluate these models to other spatial scales different from those targeted in their development (Yang et al., 2014; Zipper and Lohede, 2014; Bisquert et al., 2016; Ortega-Farias et al., 2016, 2017), as the change in the spatial resolution could impact on the turbulent heat fluxes calculation, resulting in a spatial scale discrepancy (Su et al., 1999).

Several authors have studied the effect of the spatial resolution of input satellite data on  $ET_c$  estimation. Thus, Su et al. (1999), Hong et al. (2009), Gebremichael et al. (2010), Long et al. (2011) and Tang et al. (2013) analyzed spatial resolution effect on SEBAL model. McCabe and Wood (2006), Ershadi et al. (2013) and Sharma et al. (2016) performed studies with the same objective than the previous ones, but based on SEBS model, whereas Tian et al. (2012) focused on the effect on METRIC model. Kustas et al. (2004) performed a similar research by using a two-source SEB model (Norman et al., 1995). All these studies were mainly focused on the range from Landsat to MODIS spatial resolutions and found that a good agreement exists between ET estimated from these satellites, especially when simple averaging approach is used for spatial input aggregation. In addition, these authors also pointed out the critical role that extreme pixels selection and land surface heterogeneity play, which can cause significant errors in the ET estimation. However, they did not assess the effect of the image pixel size on the  $ET_c$  estimation, especially when non-homogeneous crops are evaluated.

Therefore, the objective of this study was to assess the effect of spatial resolution on  $ET_c$  estimated in open-canopy olive orchards using METRIC model (Allen et al., 2007a). To achieve this objective, the study encompassed a wide range of pixel sizes (from meters to kilometers) representing the first attempt to run the METRIC model at very high spatial resolution. This objective was addressed for each component of the energy balance, assessing their corresponding sensitivities to changes in spatial resolution and evaluating the impact on the assessment of water requirements.

## 2. Materials and methods

### 2.1. Airborne campaigns

Three airborne campaigns were carried out during 2012 on 6th July (Day of Year, DOY, 188), 23rd August (DOY 236) and 8th September (DOY 252) over a large olive region (2600 ha) located between Córdoba, Málaga and Sevilla provinces (southern Spain) (37.25 °N, 4.70 °W) (Fig. 1). The area has a Mediterranean climate, with an

average annual temperature, total annual rainfall and cumulative reference evapotranspiration for 2012 of 17.1 °C, 456 and 1498 mm, respectively (Agroclimatic Information Network of Andalucía, <https://www.juntadeandalucia.es/agriculturaypesca/ifapa/ria/>).

Detailed information from a total of 192 olive plots was obtained from farmers and technicians working within the area of study (Alameda, Badolatosa, Casariche and La Roda de Andalucía municipalities; Fig. 1). Most of the fields under study were grown under rainfed conditions ( $\approx 70\%$ ) whereas 30% received some amount of irrigation water. In the area, olive planting frameworks vary between fields, but 7 m x 7 m and 8 m x 8 m were the most frequent tree spacings. The  $F_c$  of the olive orchards ranged from 13 to 47%, being the average  $F_c$  of 30%. Soil management varied among plots, but due to the period considered (summer time) most fields were without cover crops or they were dry.

The flights were realized by the Laboratory for Research Methods in Quantitative Remote Sensing (QuantaLab, IAS-CSIC, Spain) employing a hyperspectral and a thermal camera installed in a Cessna C172S aircraft.

### 2.1.1. Hyperspectral sensor

The hyperspectral sensor on board the aircraft was a micro-hyperspectral camera (Micro-Hyperspec VNIR model, Headwall Photonics, MA, USA), covering the 400–885 nm spectral region with 260 bands. The sampling interval was 1.85 nm with a radiometric resolution of 12 bit, resulting in a 6.4 nm full width half maximum (FWHM) with an entrance slit width of 25  $\mu\text{m}$ . Data acquisition and storage on the aircraft was 50 frames per second at 18 ms integration time. The focal length was 8 mm resulting in a pixel size of 40 cm. Hyperspectral images were radiometrically, atmospherically and geometrically corrected. Coefficients derived from a calibrated integrating sphere (CSTM-USS-2000C LabSphere, North Sutton, NH, US) were used to perform the radiometric calibration. The SMARTS model (Gueymard, 1995) was used to conduct the atmospheric correction, simulating the total incoming irradiance at 1 mm intervals. The geometric correction was conducted incorporating data acquired from an inertial measuring unit (IMU) on board the aircraft in PARGE (ReSe Applications Schl pfer, Wil, Switzerland). Additionally, a manual coregistration process was carried out with ArcGIS 10.2, identifying common ground control points (GCPs) both in the hyperspectral images and in orthophotos of the year 2013 obtained from the Spanish Geographic Institute ([www.ign.es](http://www.ign.es)) and used as a reference. GCPs were located according to the methodology followed by Ram rez-Cuesta et al. (2017), prioritizing locations on tree canopy centers and varying the point density according to the planting density and the size of the trees. For the transformation of the hyperspectral image to match the map coordinates of the target data, the Spline method was used. The average Root Mean Square Errors (RMSE) for DOY 188, 236 and 252 were 0.50, 0.12, and 1.56 m, respectively.

### 2.1.2. Thermal sensor

The thermal camera was a FLIR SC655 camera (FLIR SC655, FLIR System, USA) encompassing the 7.5–13  $\mu\text{m}$  spectral region and yielding a 17  $\mu\text{m}$  pixel size. The optical focal length was 13.1 mm resulting in an angular field of view of 45° and in 50 cm pixel resolution. The sensor was a Focal Plane Array (FPA) based on uncooled microbolometers. The FPA temperature, warm-up time, camera settings and the environment where the measurements are performed were considered to avoid possible errors (Leinonen et al., 2006; Berni et al., 2009a; Zia et al., 2010; Kusnerek and Korsath, 2014). The thermal camera acquired and stored on board the aircraft uncalibrated 16 bit digital raw images being previously radiometrically calibrated in the laboratory utilizing a blackbody (model P80 P, Land Instruments, Dronfield United Kingdom). In addition, a range of field calibrations were conducted measuring the surface temperature ( $T_s$ ) with a thermal gun (LaserSight, Optris, Germany) at the time of the flights. The resulting Root Mean

Square Error (RMSE) was less than 1 K (Berni et al., 2009a, b). The same manual coregistration process carried out to the hyperspectral images was conducted on the thermal imagery to correct the inherent imagery deformation caused by motions of the aircraft (pitch, roll and yaw) and by sensor characteristics and viewing geometry (variation in sensor mechanics, viewing angles and panoramic effect with field of view). The average RMSE for DOY 188, 236 and 252 were 0.07, 0.06, and 0.03 m, respectively.

## 2.2. METRIC model

Mapping EvapoTranspiration at high Resolution with Internalized Calibration (METRIC; Allen et al., 2007a) is a satellite-based model that estimates ET from satellite imagery by applying a SEB. It calculates ET as a residual of the surface energy equation.

$$LE = R_n - G - H \quad (1)$$

where LE is the latent heat flux ( $\text{W m}^{-2}$ );  $R_n$  is the net radiation flux ( $\text{W m}^{-2}$ ); G is the soil heat flux ( $\text{W m}^{-2}$ ); and H is the sensible heat flux ( $\text{W m}^{-2}$ ).

The  $R_n$  component reflects the energy available at the surface and it is determined by subtracting the outgoing radiant components from the incoming ones.

$$R_n = R_{S\downarrow} - \alpha R_{S\downarrow} + R_{L\downarrow} - R_{L\uparrow} - (1 - \epsilon_0) R_{L\downarrow} \quad (2)$$

where  $R_{S\downarrow}$  is the incoming shortwave radiation ( $\text{W m}^{-2}$ ),  $\alpha$  is the surface albedo (dimensionless) defined as the ratio of the reflected solar radiation to the incident solar (short-wave) radiation at the surface,  $R_{L\downarrow}$  is the incoming longwave radiation ( $\text{W m}^{-2}$ ),  $R_{L\uparrow}$  is the outgoing longwave radiation ( $\text{W m}^{-2}$ ), and  $\epsilon_0$  is the surface thermal emissivity (dimensionless).

A comparison between field-measured and satellite derived  $\alpha$  was carried out. The purpose was to check the performance under conditions of southern Spain of the methodology for assessing  $\alpha$  using the weighting coefficients ( $W_b$ ) proposed by Tasumi et al. (2008) (Table 1S).

G represents the heat conducted into soil and it is determined using an empirical equation developed by Tasumi et al. (2003).

$$G = R_n (0.05 + 0.18e^{-0.52LAI}) \quad LAI \geq 0.5 \quad (3a)$$

$$G = R_n \left( \frac{1.80(T_s - 273.16)}{R_n} + 0.084 \right) \quad LAI < 0.5 \quad (3b)$$

where  $T_s$  is the surface temperature (in Kelvin) and LAI is the leaf area index estimated within the METRIC approach using an empirical equation dependent on Soil Adjusted Vegetation Index, SAVI (Allen et al., 2012), calculated from the red and near infrared bands (Huete, 1988).

H considers the energy convected and conducted to the air due to temperature differences. In METRIC, H is calculated from the difference between the surface aerodynamic temperature and a reference height air temperature (Brutsaert, 1982).

$$H = \rho C_p \frac{dT}{r_{ah}} \quad (4)$$

where  $\rho$  is the air density ( $\text{kg m}^{-3}$ );  $C_p$  is the air specific heat at a constant pressure ( $1004 \text{ J kg}^{-1} \text{ K}^{-1}$ ),  $r_{ah}$  is the aerodynamic resistance to heat transfer ( $\text{s m}^{-1}$ ), and  $dT$  is the near surface temperature gradient between two near surface heights (K), calculated as a linear function of  $T_s$  as indicated Bastiaanssen (1995).

$$dT = a + bT_{s, datum} \quad (5)$$

where a and b are empirically estimated constants for each satellite image using two anchor pixels (referred as hot and cold pixels), and  $T_{s, datum}$  is the surface temperature adjusted to a common elevation datum using a digital elevation model and a specified lapse rate (Allen et al.,

2007a).

Once all the components included in Eq. (1) are determined, ET at the instant of the satellite image is calculated for each pixel by dividing LE from Eq. (1) by latent heat of vaporization

$$ET_{inst} = 3,600 \frac{LE}{\lambda \rho_w} \quad (6)$$

where  $ET_{inst}$  is the instantaneous ET ( $\text{mm h}^{-1}$ );  $\rho_w$  represents the density of water ( $1000 \text{ kg m}^{-3}$ ); and  $\lambda$  is the latent heat of vaporization ( $\text{J kg}^{-1}$ ).

A full description of the processes included in the METRIC model can be found in Allen et al. (2007a).

### 2.3. Validation of METRIC derived albedo determined using Landsat scenes

In order to estimate  $R_n$  the accurate estimation of  $\alpha$  is critical. Broad-band  $\alpha$  is calculated by integrating the at-surface reflectivities from representative satellite bands (e.g. bands 1–5 and 7 of Landsat 7; bands 1–7 of MODIS; and bands 1–9 of ASTER) using a weighting function:

$$\alpha_s = \sum_{b=1}^n [\rho_{s,b} W_b] \quad (7)$$

where  $\rho_{s,b}$  is the at-surface reflectance for band  $b$ ,  $W_b$  is a weighting coefficient (Table 1S) representing the fraction of at-surface solar radiation occurring within the spectral range represented by a specific band, and  $n$  is the number of satellite bands integrated.

A comparison between field measured and satellite derived  $\alpha$  was performed to evaluate the validity of  $W_b$  for Spain. Thus, two albedometers (Hukseflux SRA01, Hukseflux Thermal Sensors B.V., The Netherlands) were installed from March to September 2015, in a 22 ha olive grove with a tree spacing of  $12 \times 10 \text{ m}$  in Montilla (Córdoba, Spain) (Fig. 2). One of them was placed 0.2 m over the tree canopy to ensure the instrument measurement corresponded purely with the canopy olive  $\alpha$ , whereas the second one was located 0.3 m over the bare soil to consider only this surface (Fig. 2). Once the olive and bare soil  $\alpha$  components were measured, they were weighted using the canopy  $F_c$  to assess the total  $\alpha$  value corresponding to the  $30 \times 30 \text{ m}$  Landsat pixel where the field  $\alpha$  measurements were made. During the considered period, some precipitation events took place, which helped to extend the range of  $\alpha$  measured since these events modified the color of the

underlying soil.

Satellite derived  $\alpha$  was obtained from eleven free-clouds images from Landsat 7 and Landsat 8 satellites using Eq. (7) with the  $W_b$  values proposed by Tasumi et al. (2008) and described in Table 1S. The dates considered, and the corresponding satellite overpasses are included in Table 2S.

### 2.4. Calculation of surface albedo using high resolution hyperspectral and thermal images

Hyperspectral imagery acquired by the Micro-Hyperspec VNIR camera has a spectral resolution (56 VIS/IR bands ranging between 0.4–0.8  $\mu\text{m}$ ) different from Landsat 7/8 spectral resolution (6–7 VIS/IR bands ranging between 0.4–2.4  $\mu\text{m}$ ). It means that the spectral range encompassed by bands 5 and 7 of Landsat 7 and bands 6 and 7 of Landsat 8 is not covered by the hyperspectral data. Then, the original  $W_b$  proposed by Tasumi et al. (2008) for Landsat  $\alpha$  estimation had to be adjusted when using the above described hyperspectral images (Table 1S). Thus, four approaches were considered to reproduce the  $\alpha$  calculated at the satellite level, solving the previously described limitations (Table 1S).

### 2.5. METRIC application with high resolution hyperspectral and thermal imagery

In order to assess the effects of spatial resolution on  $ET_c$  assessment, the original  $0.5 \times 0.5 \text{ m}$  spatial resolution hyperspectral and thermal images were resampled to coarser resolutions using as aggregation technique the mean of all cells encompassed by the output pixel extent. The minimum spatial resolution was fixed by analyzing the maximum average error committed during the georeferencing process; whereas the maximum spatial resolution matches the resolution of MODIS satellite. Thus, the spatial resolutions  $5 \times 5 \text{ m}$ ,  $10 \times 10 \text{ m}$ ,  $15 \times 15 \text{ m}$ ,  $20 \times 20 \text{ m}$ ,  $25 \times 25 \text{ m}$ ,  $30 \times 30 \text{ m}$ ,  $60 \times 60 \text{ m}$ ,  $100 \times 100 \text{ m}$ ,  $250 \times 250 \text{ m}$ ,  $500 \times 500 \text{ m}$  and  $1000 \times 1000 \text{ m}$  were evaluated. For comparison between the results obtained at different pixel sizes, Landsat 7 and 8 spatial resolution ( $30 \times 30 \text{ m}$  in visible bands for L7 and L8; and  $60 \times 60 \text{ m}$  for L7 and  $100 \times 100 \text{ m}$  for L8, in thermal Infrared band) was selected as the reference, since METRIC model has been widely used at this scale with satisfactory performance (Allen et al., 2007a, b; Santos et al., 2008, 2012; Paço et al., 2014; De la Fuente-Sáiz et al., 2017). In terms of plot average, all pixels totally or

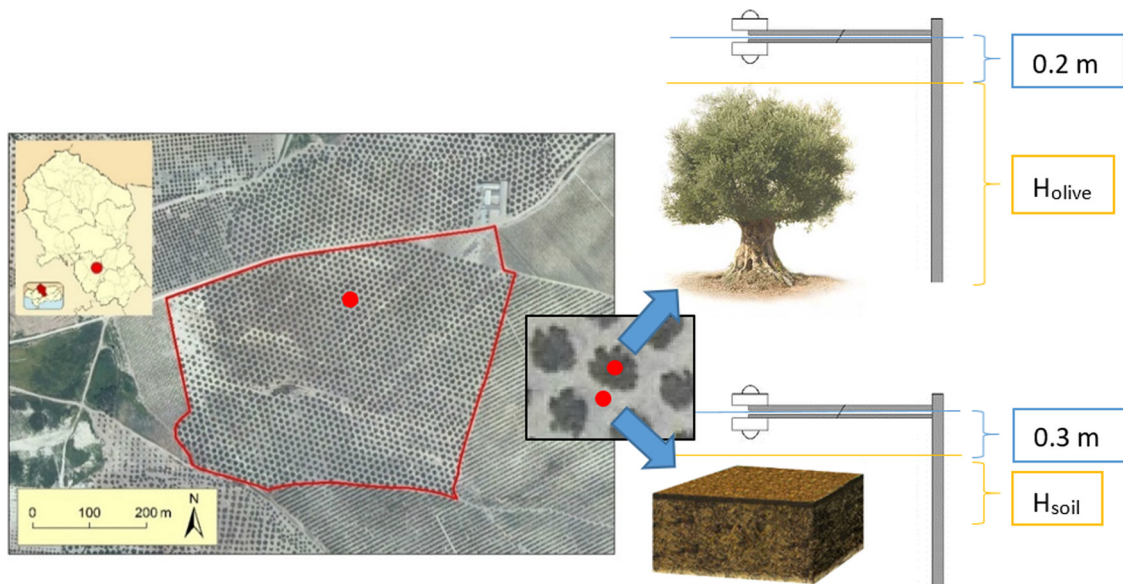


Fig. 2. Olive grove where  $\alpha$  measurements were taken (left) and albedometers installation scheme (right).

partially included in the plots were taken into account for the computation.

### 2.6. Hot and cold pixel selection

One of the most important tasks for an accurate  $ET_c$  assessment using METRIC is the correct selection of the hot and cold pixel (Allen et al., 2007a). However, the area covered by the flights lacks well-watered and fully vegetated fields that can be considered as cold pixel. Thus, an alternative method to calibrate METRIC model was conducted.

First, hot and cold pixels were identified in surrounding areas of the analyzed region, within the Landsat scene corresponding to each flight date. Once the cold and hot pixels were selected on the Landsat images, their corresponding temperatures on the airborne derived images was calculated based on the temporal dependent relationship between the temperature derived from the Landsat scenes and the temperature acquired from the airborne (Ramírez-Cuesta et al., 2017). These corrected temperatures will be used to derive the near  $dT$  defined in Eq. (5).

## 3. Results

### 3.1. Surface albedo validation (Landsat derived vs. field measurements)

Results from the comparison between the field measurements of  $\alpha$  and the satellite estimated  $\alpha$  are shown in Fig. 3. Olive grove  $\alpha$  during the campaign ranged from 0.14 to 0.24. Pure canopy  $\alpha$  was nearly constant ranging from 0.14 to 0.17 whereas the pure bare soil  $\alpha$  exhibited greater variation, with values ranging from 0.14 to 0.27.

In general, a good relationship between the measured and the Landsat derived  $\alpha$  was observed (Fig. 3), with a mean error of 8.4% for the period considered, reaching a maximum error of 18% for the DOY 148. Fig. 3 shows that using  $W_b$  values proposed by Tasumi et al. (2008), an underestimation of Landsat derived  $\alpha$  was found when measured  $\alpha$  was lower than around 0.19 whereas an overestimation occurred when the measured  $\alpha$  was greater than 0.19. From these results,  $\alpha$  derived using  $W_b$  values proposed by Tasumi et al. (2008) can be adjusted for olive groves under Mediterranean conditions using the empirical equation derived from the measured and estimated  $\alpha$ .

$$\alpha_{adj} = 0.5734 \alpha_0 + 0.0808 \quad (8)$$

where  $\alpha_0$  is the  $\alpha$  estimated using  $W_b$  values proposed by Tasumi et al. (2008).

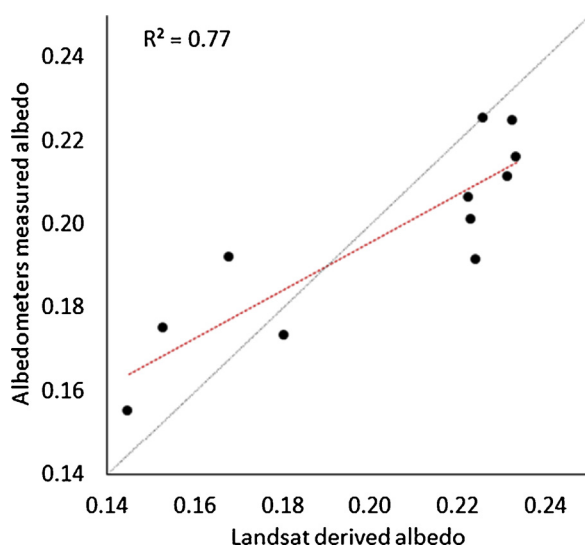


Fig. 3. Field  $\alpha$  measurements and Landsat  $\alpha$  estimates comparison (dashed black line represents the 1:1 relationship).

### 3.2. Surface albedo from hyperspectral data

The relationships between  $\alpha$  derived from Tasumi coefficients and coefficients for hyperspectral data (Table 1S) are shown in Fig. 4. Although all approaches show a near 1:1 relationship, the best relationship corresponds with Approach 4 (band 7 coefficient was added to band 4 coefficient and band 5 coefficient was added to band 3 coefficient; Table 1S) depicting the lowest scatter ( $R^2 = 0.9934$ ).

### 3.3. METRIC application on hyperspectral and thermal imagery at different spatial resolutions

#### 3.3.1. Net radiation

Average  $R_n$  value for the total 192 fields and considering the  $30 \times 30$  m spatial resolution was 487.82, 425.84 and 417.62  $W m^{-2}$  for DOY 188, 236 and 252, respectively. However, these values for the same fields varied according to the considered spatial resolution (Tables 1–3). For DOY 188, mean  $R_n$  value ranged between 99.43 and 103.59% of  $30 \times 30$  m  $R_n$  value depending on the spatial resolution considered, with the highest overestimation for  $1000 \times 1000$  m resolution (Table 1). For DOY 236, the average value of  $R_n$  varied from 95.43 to 103.40% regarding the  $30 \times 30$  m spatial resolution (Table 2), while for DOY 252 these values ranged between 97.41 and 105.88% (Table 3). It implies that, considering the three dates,  $R_n$  oscillated  $\pm 6\%$  from the  $30 \times 30$  m values. Fig. 5 shows an example of the  $R_n$  spatial distribution in a fragment of the study area for the different spatial resolutions for DOY 188. Regarding the existing variability among the different plots, it was practically the same for all spatial resolutions, with standard deviations (SD) ranging from 21.95 to 37.08  $W m^{-2}$ .

The limited impact of spatial resolution on  $R_n$  was also observed when plotting  $R_n$  at different spatial resolutions versus  $R_n$  at  $30 \times 30$  m spatial resolution (Fig. 6). The regression obtained for all pixel sizes are close to the 1:1 relationship (slope varying from 0.97 to 1.04; Table 4). However, the  $R^2$  value worsened as the pixel size moved away from  $30 \times 30$  m, being divergences more evident when coarser spatial resolutions were considered, reaching  $R^2$  values around 0.30 for  $500 \times 500$  m and  $1000 \times 1000$  m pixel sizes (Table 4). However, with resolution up to  $60 \times 60$  m  $R^2$  values were around 0.90 (Table 4).

#### 3.3.2. Soil heat flux

Average  $G$  values for the 192 fields determined from METRIC at  $30 \times 30$  m spatial resolution were 75.70, 64.34 and 69.77  $W m^{-2}$  for DOY 182, 236 and 252, respectively (Tables 1–3). The mean  $G$  value ranged from 97.90 to 106.53%, from 95.26 to 102.68% and from 94.37 to 103.19% regarding the  $30 \times 30$  m resolution value, for DOY 188, 236 and 252 (Tables 1–3), respectively. Summing up the three dates,  $G$  values ranged between 94% and 107% compared with  $30 \times 30$  m resolution value. Fig. 7 shows the  $G$  obtained with the different resolutions for DOY 188 in a portion of the study area. The variability observed in the study area was very constant for all pixels sizes, with SD ranging from 3.23 to 9.05  $W m^{-2}$ .

The mean value oscillation due to spatial resolution changes is very similar to the pattern observed in  $R_n$ . The regression lines observed in Fig. 6 followed a near 1:1 trend (slope ranging from 0.97 to 1.05; Table 4) with the highest  $R^2$  at medium resolutions (from 15 to 25 m pixel sizes), getting worse as the spatial resolutions moves away from this medium resolutions, being more evident for spatial resolution coarser than  $100 \times 100$  m.

#### 3.3.3. Sensible heat flux

The mean  $H$  values observed for DOY 188, 236 and 252 at  $30 \times 30$  m spatial resolution were 161.12, 125.11 and 157.58  $W m^{-2}$ , respectively (Tables 1–3). However,  $H$  showed a greater variation when spatial resolution changed. Thus,  $H$  oscillated between 83.06 and 100.37% for DOY 188 (Table 1); between 90.61 and 99.82% for DOY

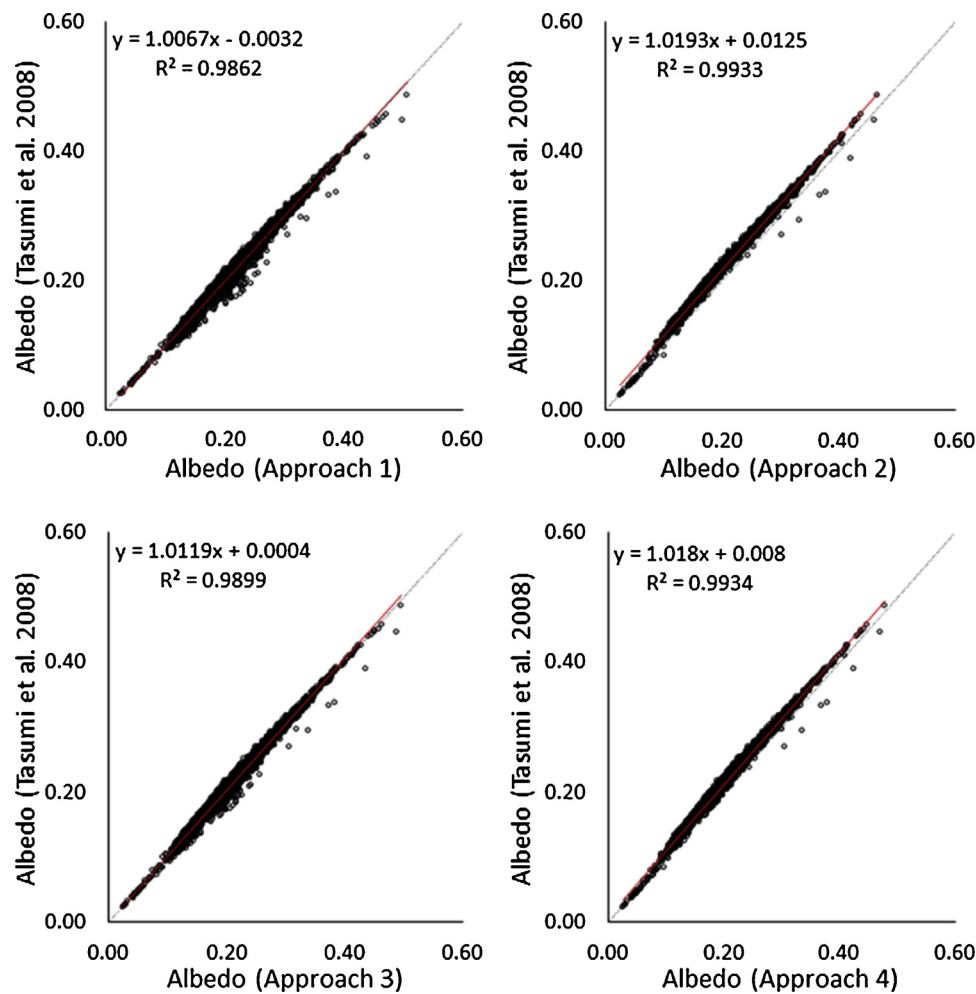


Fig. 4. Relationship between  $\alpha$  estimated from Tasumi coefficients and using alternative  $W_b$  for hyperspectral images described in Table 1S.

Table 1

Mean, maximum, minimum and standard deviation plot values of the SEB components (and  $K_{co}$ ) for the different spatial resolutions of DOY 188. Bold values in the table refer to the values for the spatial resolution taken as reference (30 x 30 m).

Pixel Size (m)	$R_n$ ( $W m^{-2}$ )				$G$ ( $W m^{-2}$ )				$H$ ( $W m^{-2}$ )				$ET_c$ (mm)				$K_{co}$ (-)			
	Mean	Max	Min	SD	Mean	Max	Min	SD	Mean	Max	Min	SD	Mean	Max	Min	SD	Mean	Max	Min	SD
5 x 5	488.44	548.22	396.95	30.82	80.64	95.44	65.89	5.10	161.72	231.55	91.80	24.38	3.52	5.27	1.74	0.61	0.54	0.81	0.27	0.09
10 x 10	488.09	547.54	388.65	31.24	75.72	91.37	63.36	4.59	159.70	249.98	89.20	24.42	3.59	5.31	1.67	0.61	0.55	0.82	0.26	0.09
15 x 15	490.99	543.32	421.24	27.34	76.09	99.85	65.45	4.71	159.07	244.12	99.03	24.18	3.63	4.94	1.82	0.55	0.56	0.76	0.28	0.08
20 x 20	490.64	541.49	422.21	27.06	75.94	122.96	65.68	5.63	159.56	307.41	104.04	25.45	3.62	4.77	1.64	0.58	0.56	0.73	0.25	0.09
25 x 25	490.74	552.75	393.15	27.65	75.83	100.13	63.00	4.95	159.62	252.70	102.98	24.23	3.63	4.79	0.80	0.57	0.56	0.74	0.12	0.09
<b>30 x 30</b>	<b>487.82</b>	<b>545.18</b>	<b>391.24</b>	<b>28.55</b>	<b>75.70</b>	<b>104.77</b>	<b>65.69</b>	<b>5.22</b>	<b>161.12</b>	<b>261.93</b>	<b>109.45</b>	<b>24.19</b>	<b>3.56</b>	<b>4.72</b>	<b>1.25</b>	<b>0.58</b>	<b>0.55</b>	<b>0.73</b>	<b>0.19</b>	<b>0.09</b>
60 x 60	488.11	553.94	406.07	25.68	75.38	99.34	60.91	4.64	149.91	236.99	100.19	24.20	3.73	5.22	2.19	0.53	0.57	0.80	0.34	0.08
100 x 100	490.13	578.89	411.23	25.46	75.45	91.75	61.68	4.10	146.99	229.38	94.60	24.52	3.80	5.62	2.13	0.55	0.58	0.86	0.33	0.09
250 x 250	487.03	550.63	414.70	23.63	74.11	89.13	62.20	3.96	143.77	211.51	83.42	24.24	3.82	5.20	2.50	0.51	0.59	0.80	0.39	0.08
500 x 500	485.04	560.39	410.96	34.36	74.56	89.58	61.64	5.70	146.60	223.96	96.90	24.32	3.75	5.02	2.01	0.66	0.58	0.77	0.31	0.10
1000 x 1000	505.35	550.60	450.07	26.95	77.84	103.94	67.51	6.02	133.82	259.84	72.08	46.70	4.16	4.98	1.43	0.82	0.64	0.77	0.22	0.13

236 (Table 2); and between 89.20 and 99.82% for DOY 252 (Table 3), when compared with 30 x 30 m spatial resolution H values. H determined for the different spatial resolutions are shown in Fig. 8. The variability observed among the plots varied in function of the day. Thus, for DOY 236 the SD was lower (13.25–20.19  $W m^{-2}$ ) than for DOY 188 and 252 (24.18–46.70  $W m^{-2}$ ). However, for the three dates, the SD was greater at very coarse pixel sizes (1000 x 1000 m) than for finer resolutions.

The linear regressions obtained by the comparison between

different spatial resolutions and 30 x 30 m pixel size (Fig. 6 and Table 4) showed that H is more sensitive to upscaling process (spatial resolution coarser than 30 x 30 m showed slopes ranging from 0.90 to 0.93 and  $R^2$  values reaching 0.16) whereas for high spatial resolution, the regression was close to line 1:1, with  $R^2$  values higher than 0.90 (Table 4).

### 3.3.4. Crop evapotranspiration and crop coefficient

Average  $ET_c$  values for 30 x 30 m spatial resolution were 3.56 mm

**Table 2**

Mean, maximum, minimum and standard deviation plot values of the SEB components (and  $K_{co}$ ) for the different spatial resolutions of DOY 236. Bold values in the table refer to the values for the spatial resolution taken as reference (30 x 30 m).

Pixel Size (m)	$R_n$ ( $W m^{-2}$ )				G ( $W m^{-2}$ )				H ( $W m^{-2}$ )				$ET_c$ (mm)				$K_{co}$ (-)			
	Mean	Max	Min	SD	Mean	Max	Min	SD	Mean	Max	Min	SD	Mean	Max	Min	SD	Mean	Max	Min	SD
5 × 5	425.66	480.90	357.08	26.53	65.94	75.55	55.11	3.52	124.89	166.42	82.47	13.80	3.55	4.64	2.28	0.44	0.48	0.63	0.31	0.06
10 × 10	425.71	479.92	346.52	26.35	64.56	72.08	52.49	3.56	124.58	166.40	83.35	13.63	3.58	4.58	2.30	0.42	0.49	0.62	0.31	0.06
15 × 15	425.76	477.08	358.71	25.29	64.40	72.15	54.78	3.48	124.35	165.28	84.30	13.50	3.59	4.45	2.31	0.41	0.49	0.60	0.31	0.06
20 × 20	425.69	476.06	358.74	24.66	64.30	71.63	54.65	3.41	124.54	164.79	87.36	13.25	3.59	4.39	2.27	0.39	0.49	0.60	0.31	0.05
25 × 25	425.68	475.78	351.18	24.43	64.29	73.54	52.68	3.42	124.67	164.53	86.00	13.45	3.59	4.35	2.15	0.39	0.49	0.59	0.29	0.05
<b>30 × 30</b>	<b>425.84</b>	<b>474.19</b>	<b>350.76</b>	<b>24.34</b>	<b>64.34</b>	<b>74.33</b>	<b>52.61</b>	<b>3.40</b>	<b>125.11</b>	<b>170.26</b>	<b>90.67</b>	<b>13.43</b>	<b>3.58</b>	<b>4.35</b>	<b>2.12</b>	<b>0.39</b>	<b>0.49</b>	<b>0.59</b>	<b>0.29</b>	<b>0.05</b>
60 × 60	424.86	479.79	328.66	23.21	64.18	72.76	49.30	3.31	115.36	151.91	74.07	14.04	3.72	4.66	2.45	0.38	0.51	0.63	0.33	0.05
100 × 100	425.55	483.84	349.35	21.95	64.20	72.58	52.40	3.23	113.36	160.61	59.37	16.09	3.76	4.75	2.73	0.40	0.51	0.65	0.37	0.05
250 × 250	421.08	483.49	341.69	27.17	63.55	72.52	51.25	4.00	113.45	161.11	71.63	16.17	3.70	4.89	2.40	0.47	0.50	0.66	0.33	0.06
500 × 500	406.36	498.95	327.84	37.08	61.29	74.84	50.71	5.39	116.10	151.86	58.15	14.92	3.47	5.27	2.16	0.59	0.47	0.72	0.29	0.08
1000 × 1000	440.31	503.86	358.83	22.44	66.06	75.58	54.35	3.33	122.80	169.45	86.05	20.19	3.81	4.68	2.56	0.36	0.52	0.64	0.35	0.05

**Table 3**

Mean, maximum, minimum and standard deviation plot values of the SEB components (and  $K_{co}$ ) for the different spatial resolutions of DOY 252. Bold values in the table refer to the values for the spatial resolution taken as reference (30 x 30 m).

Pixel Size (m)	$R_n$ ( $W m^{-2}$ )				G ( $W m^{-2}$ )				H ( $W m^{-2}$ )				$ET_c$ (mm)				$K_{co}$ (-)			
	Mean	Max	Min	SD	Mean	Max	Min	SD	Mean	Max	Min	SD	Mean	Max	Min	SD	Mean	Max	Min	SD
5 × 5	417.70	495.72	314.63	35.73	72.00	87.18	50.61	6.18	157.29	253.63	80.84	34.45	1.86	3.09	0.48	0.54	0.43	0.71	0.11	0.13
10 × 10	418.39	504.59	315.55	35.05	70.01	86.95	50.54	6.81	156.93	246.78	80.05	33.71	1.90	3.10	0.48	0.55	0.44	0.72	0.11	0.13
15 × 15	418.54	493.00	324.90	31.77	69.35	84.26	53.90	6.40	154.04	246.77	79.15	30.40	1.93	3.04	0.72	0.49	0.45	0.70	0.17	0.11
20 × 20	416.99	496.44	313.48	33.04	69.55	88.11	55.78	7.02	156.32	250.58	75.53	31.83	1.89	3.09	0.53	0.53	0.44	0.71	0.12	0.12
25 × 25	416.49	495.84	320.94	33.38	69.58	88.86	50.57	7.23	156.03	250.44	76.53	31.65	1.89	3.07	0.53	0.53	0.44	0.71	0.12	0.12
<b>30 × 30</b>	<b>417.62</b>	<b>498.46</b>	<b>312.57</b>	<b>32.07</b>	<b>69.77</b>	<b>89.75</b>	<b>50.25</b>	<b>7.23</b>	<b>157.58</b>	<b>249.54</b>	<b>73.11</b>	<b>31.54</b>	<b>1.88</b>	<b>3.08</b>	<b>0.53</b>	<b>0.52</b>	<b>0.43</b>	<b>0.71</b>	<b>0.12</b>	<b>0.12</b>
60 × 60	417.06	502.07	317.19	33.36	68.90	95.29	49.18	7.19	144.41	238.22	45.09	35.12	2.01	3.42	0.46	0.56	0.46	0.79	0.11	0.13
100 × 100	414.65	488.92	333.97	33.41	68.06	94.76	52.50	6.96	144.92	270.74	38.11	34.40	1.99	3.26	0.42	0.54	0.46	0.75	0.10	0.12
250 × 250	408.97	495.73	312.62	31.22	66.86	87.13	52.54	6.17	141.30	242.82	63.41	32.21	1.99	3.24	0.64	0.54	0.46	0.75	0.15	0.12
500 × 500	406.81	479.51	306.27	35.37	65.84	93.60	46.26	9.05	147.72	234.00	87.27	31.96	1.91	2.71	0.69	0.46	0.44	0.63	0.16	0.11
1000 × 1000	442.18	483.13	360.87	24.12	69.38	94.44	58.37	5.58	140.56	236.10	70.26	42.57	2.30	3.23	1.26	0.54	0.53	0.75	0.29	0.13

for DOY 188; 3.58 mm for DOY 236 and 1.88 mm for DOY 252, corresponding with crop coefficients ( $K_{co}$ ) of 0.55, 0.49 and 0.43, respectively (Tables 1–3). Changes in pixel size also affected to  $ET_c$  assessment. Thereby,  $ET_c$  varied between 98.88 and 116.85% for DOY 188 (Table 1); between 96.93 and 106.42% for DOY 236 (Table 2); and between 98.94 and 122.34% for DOY 252 (Table 3), compared with the average value obtained with a 30 × 30 m spatial resolution. Figs. 9 and 10 show  $ET_c$  and  $K_{co}$  estimations derived from METRIC for the different spatial resolutions considered in this study for DOY 188. The  $K_{co}$  variability among fields was not severely affected by changes in spatial resolution, with SD values ranging from 0.05 to 0.13 for all considered pixel sizes.

As occurred with H, LE is more affected by upscaling processes than by downscaling processes. Thus, the slopes of the regression lines ranged from 0.98 to 1.09 for pixel sizes greater than 30 × 30 m; whereas for pixel sizes lower than 30 × 30 m the slope values ranged between 0.98 and 1.01 (Fig. 6 and Table 4). The same pattern is observed when the  $R^2$  value is assessed. For coarse resolutions (higher than 30 × 30 m),  $R^2$  oscillated between 0.53 and 0.90, whereas for finer resolutions (lower than 30 × 30 m),  $R^2$  value was always greater than 0.92 (Table 4).

#### 4. Discussion

Most of the processes related to land-atmosphere interactions do not respond linearly to changes in scale (Harvey, 2000; Bugmann et al., 2000; Sharma et al., 2016). In addition, heterogeneity of the land surface makes scaling process more complicated (Famiglietti and Wood, 1994; Giorgi, 1997; Su et al., 1999; Brunsell and Gillies, 2003; Sridhar

et al., 2003; Brunsell, 2011). For this reason, models that study land-atmosphere interactions may be subjected to spatial scale thresholds to avoid problems in scaling procedures (Schulze, 2000; Wallender and Grismer, 2002; Lorite et al., 2005). The effect of pixel size on SEB components estimated by METRIC model was assessed in this study, concluding that the coarse spatial resolutions poses challenges and difficulties that are potentially solved when high resolution imagery is used. Thus, spatial resolutions coarser than 60 × 60 m generated large divergences compared with results provided by traditional spatial resolutions and then, must be considered with caution. These results imply that satellite-based estimates, such as from MODIS, could yield divergences of around 20% for ET assessments in heterogeneous crops. On the other hand, results obtained at high spatial resolutions showed that there is not a critical effect on  $ET_c$  assessment, even in heterogeneous systems as olive orchards.

Evaluating specifically each SEB component, the low variation observed in  $R_n$  values at different pixel sizes indicated that  $R_n$  is quite insensitive to spatial resolution changes, both up-scaling and down-scaling processes. These results agree with assessments from other authors as Su et al. (1999); Sridhar et al. (2003); Ershadi et al. (2013) and Sharma et al. (2016), who obtained discrepancies of less than 10% in  $ET_c$  estimation when varying the spatial resolution from tens of meters to hundreds of kilometers. Equally, Kustas et al. (2004) observed that SEB components at different scales remained virtually the same, suggesting that minor errors are incurred during the scaling process.

$\epsilon_0$  and  $\alpha$  are not severely affected by changes in pixel size (Liang, 2000; Ershadi et al., 2013; Sharma et al., 2016) due to the computation of both terms are done with linear functions and then the averaged values are correct. If spatial resolution were reduced to a size able to

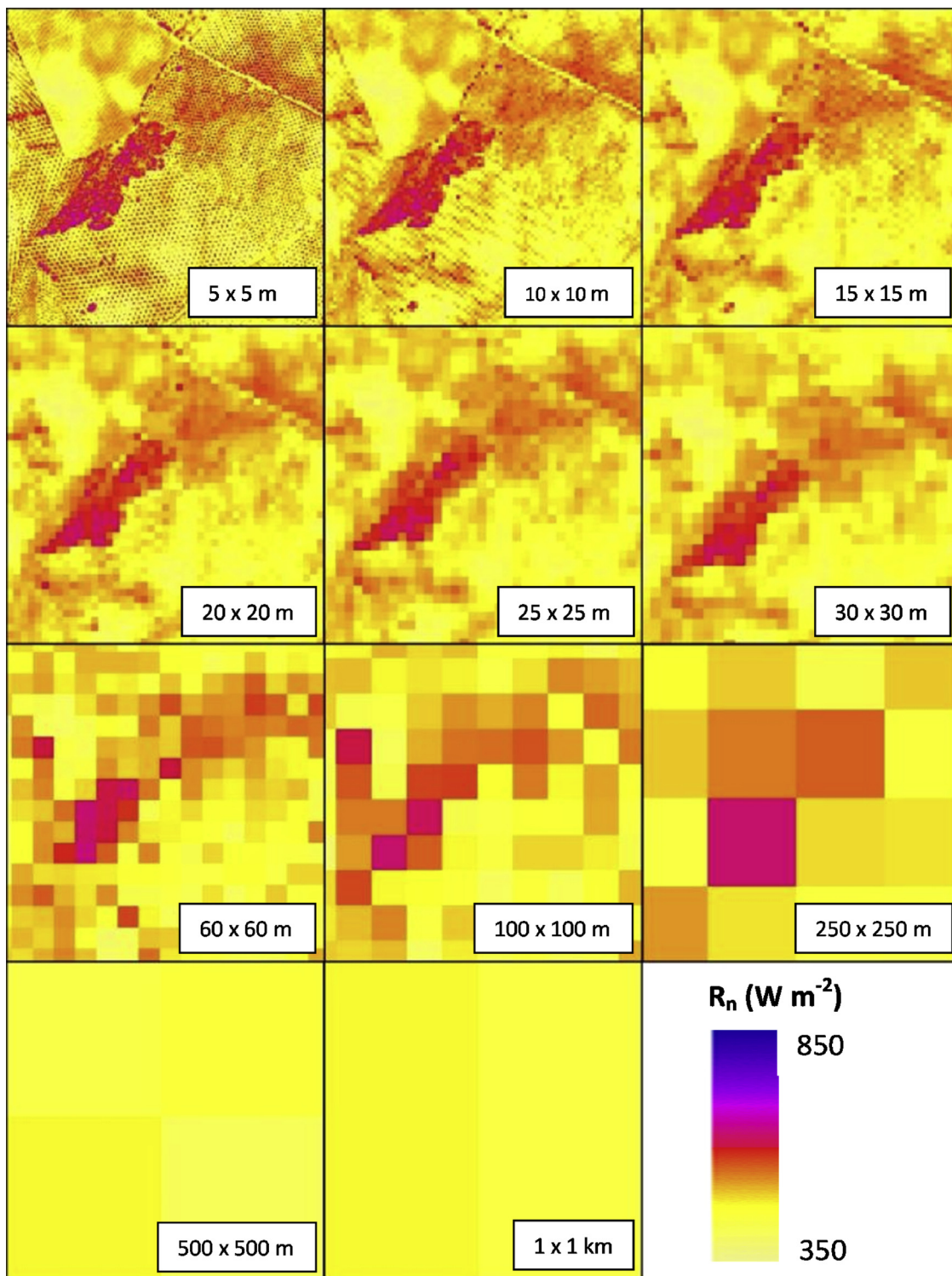


Fig. 5.  $R_n$  images derived from METRIC for DOY 188 at different spatial resolutions.

clearly differentiate trees and bare soil (e.g. 1 m) the results would be significantly different.

Additionally, in order to reduce the uncertainty in the evaluation of the impact of the spatial resolution on SEB components, a site-specific study analyzing the  $\alpha$  assessment was carried out. Thus,  $\alpha$  values measured and estimated in this study agree with the physical behavior of pure canopy and bare soil surfaces. Thus, the nearly constant trend of pure vegetation  $\alpha$  demonstrates the  $\alpha$  dependence to  $F_c$ , whereas the greater variation in the pure bare soil  $\alpha$  was due to the color change

undergone by the soil because of increased soil moisture after rainfall events. Several authors have studied the relationship between  $\alpha$  and soil moisture content, concluding that a non-linear exponential relationship exists between both variables (Idso et al., 1975b; Duke and Guérif, 1998; Lobell and Asner, 2002; Weidong et al., 2002; Roxy et al., 2010; Liu et al., 2014; Sugathan et al., 2014). Therefore, one of the main strengths of RS derived  $\alpha$  is that it considers the soil moisture content rather than using static bare soil  $\alpha$  values.

A possible explanation of the low spatial scale dependence of  $R_n$

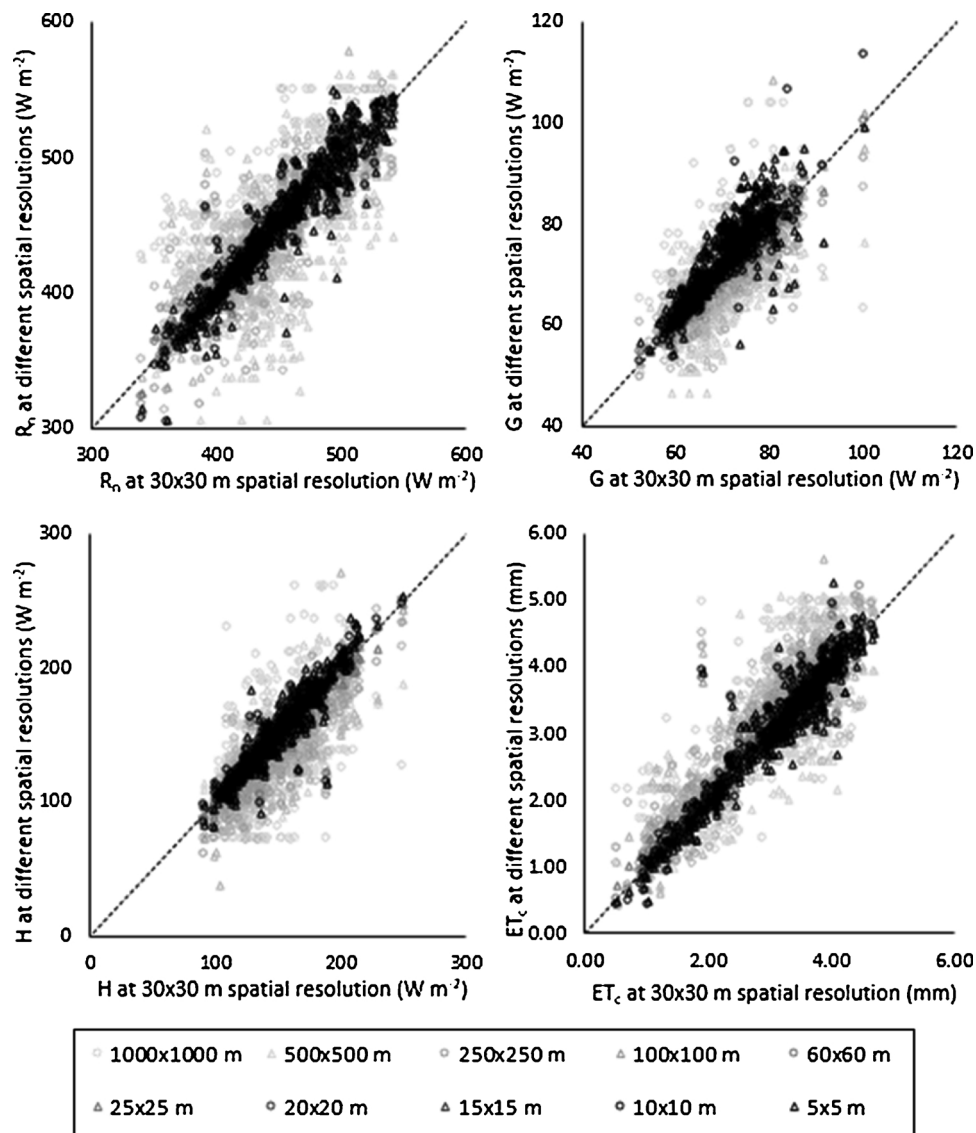


Fig. 6. Relationship between the SEB components at the different spatial resolutions and the 30 × 30 m pixel size, for DOY 188, 236 and 252. The black dashed lines represent the 1:1 relationship.

could lie in the fact that  $R_n$  is more influenced by the magnitude of incoming solar radiation than by vegetation and soil parameters (Sridhar et al., 2003) due to the low scale-variability of these parameters. In addition, although no differences should be expected in  $R_n$

since the average of the various terms in Eq. (2) are linearly combined, the low variation observed among spatial resolutions reflects the pixel contamination occurred on the edge of the fields.

Related with G, the differences due to spatial resolution changes

Table 4

Regression lines and  $R^2$  values for the relationship between the SEB components at the different pixel sizes and the 30 × 30 m pixel size.

Pixel Size (m)	$R_n$ ( $W m^{-2}$ )		G ( $W m^{-2}$ )		H ( $W m^{-2}$ )		$ET_c$ (mm)	
	Eq	$R^2$	Eq	$R^2$	Eq	$R^2$	Eq	$R^2$
5 × 5	Y = 1.00X	0.90	Y = 1.05X	0.71	Y = 1.01X	0.90	Y = 0.98X	0.92
10 × 10	Y = 1.00X	0.94	Y = 1.01X	0.90	Y = 1.00X	0.92	Y = 1.00X	0.95
15 × 15	Y = 1.00X	0.95	Y = 1.00X	0.95	Y = 0.99X	0.93	Y = 1.01X	0.95
20 × 20	Y = 1.00X	0.95	Y = 1.00X	0.96	Y = 1.00X	0.94	Y = 1.00X	0.96
25 × 25	Y = 1.00X	0.95	Y = 1.00X	0.96	Y = 1.00X	0.94	Y = 1.00X	0.97
30 × 30								
60 × 60	Y = 1.00X	0.87	Y = 0.99X	0.84	Y = 0.92X	0.85	Y = 1.04X	0.90
100 × 100	Y = 1.00X	0.82	Y = 0.99X	0.77	Y = 0.91X	0.78	Y = 1.05X	0.87
250 × 250	Y = 0.99X	0.66	Y = 0.98X	0.53	Y = 0.90X	0.62	Y = 1.04X	0.78
500 × 500	Y = 0.97X	0.29	Y = 0.97X	0.45	Y = 0.93X	0.49	Y = 0.98X	0.58
1000 × 1000	Y = 1.04X	0.35	Y = 1.02X	0.13	Y = 0.93X	0.16	Y = 1.09X	0.53

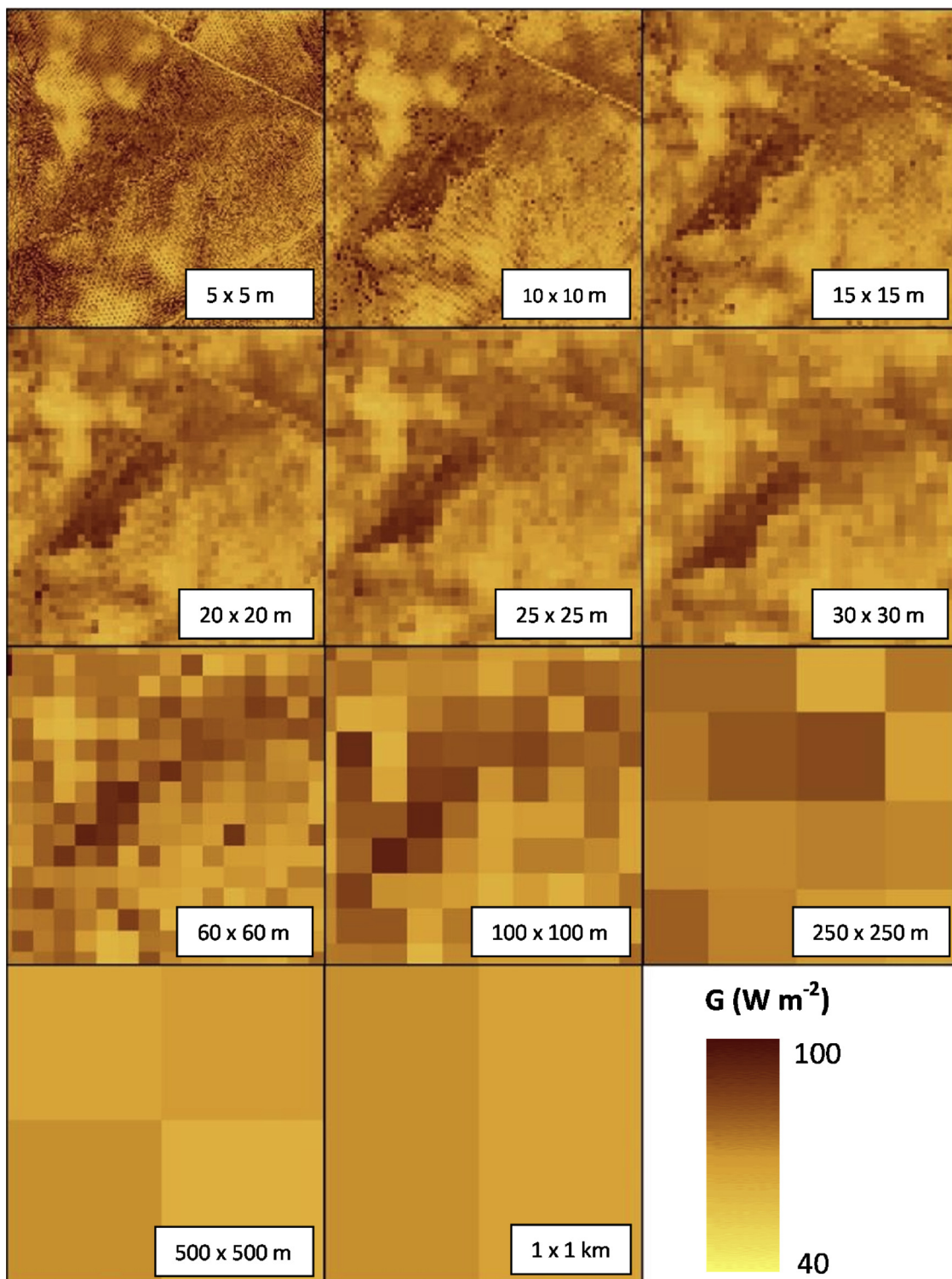


Fig. 7. G images derived from METRIC for DOY 188 at different spatial resolutions.

were very similar to the pattern observed in  $R_n$ , highlighting that G determined as METRIC does, is invariant to resolution changes. As for  $R_n$ , the small differences obtained are due to the pixel contamination at the edges of the plots. The same conclusion was obtained by Su et al. (1999), Kustas et al. (2004) and Sharma et al. (2016), the last concluding that this similar  $R_n$ -G behavior is because METRIC model uses an  $R_n$  dependent empirical equation for G calculation (Tasumi et al., 2003; Allen et al., 2007a). Greater differences were obtained by Sridhar et al. (2003), reaching discrepancies of more than 44% when spatial

resolution changed from 200 m to 20 km. These greater differences are possibly caused by the way in which NOAA-OSU Land Surface Model determines G, depending mainly on surface skin temperature instead of on  $R_n$ , as METRIC does (Allen et al., 2007a).

Referred to H the variation observed when spatial resolution changed (discrepancies ranging from 76.49 to 101.36% when compared to 30 m pixel size) was greater than the observed for  $R_n$  and G. Moreover, a significant underestimation is almost always observed when coarser than 30 × 30 m were used (relative errors up to 17%). For

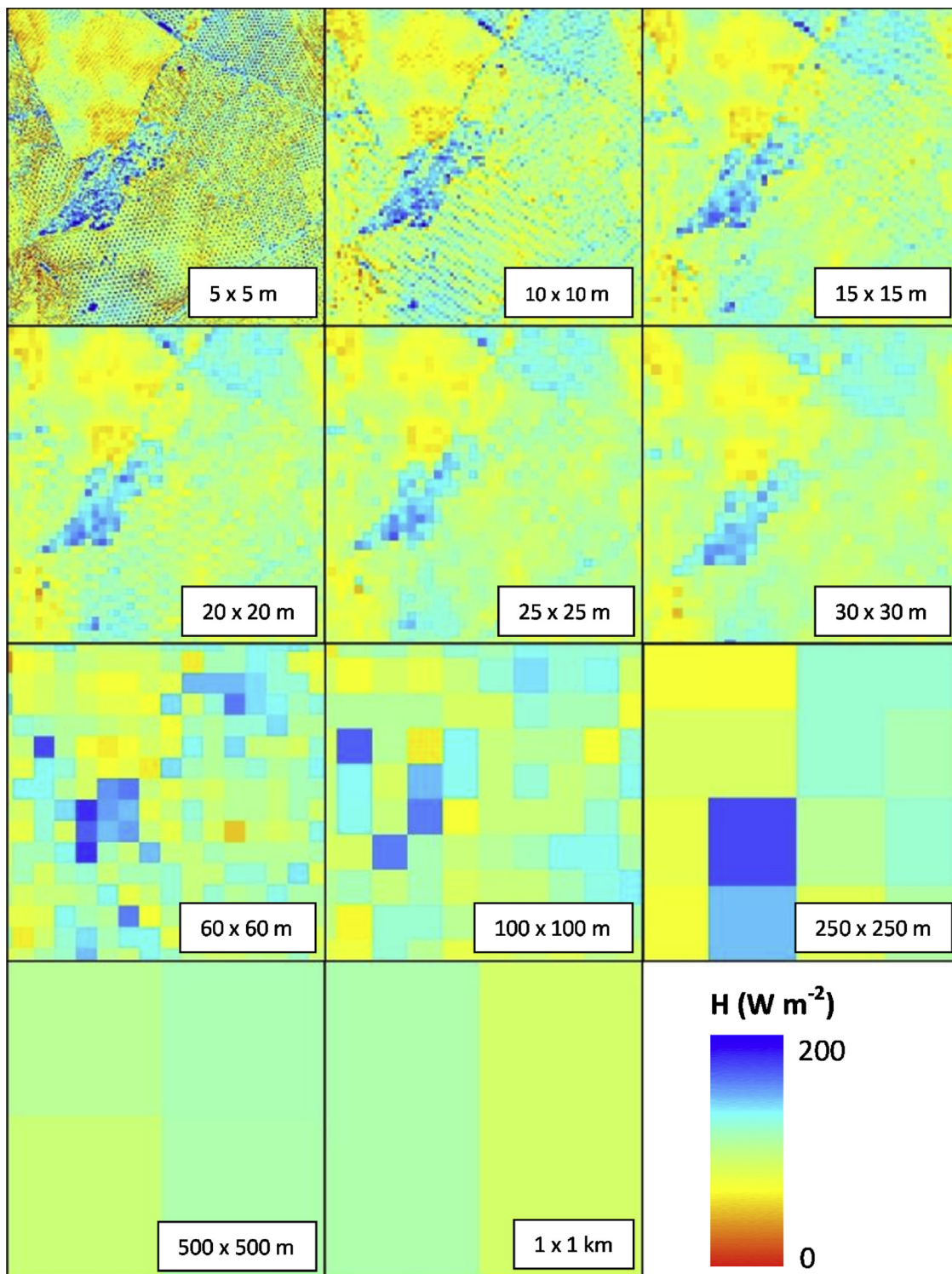


Fig. 8. H images derived from METRIC for DOY 188 at different spatial resolutions.

finer resolutions, the results were very similar to  $30 \times 30$  m pixel size (relative errors of less than 2%). These results demonstrate that H is more sensitive to changes to coarser scales whereas H does not show problems when scaling to finer resolutions. The high spatial resolution sensitivity of H could be explained by changes in  $T_s$  or in aerodynamic resistance to heat transfer (Eq. (4)). However,  $T_s$  has been proved to experience relatively small changes when modifying the scale (Tables 3S and 4S), suggesting that the aerodynamic resistance could be the main reason of H behavior to pixel size changes. Similar results have

been obtained previously by other authors using medium-coarse spatial resolutions (Moran et al., 1997; Su et al., 1999; Sridhar et al., 2003; Kustas et al., 2004; Long et al., 2011; Tang et al., 2013, and Sharma et al., 2016) who concluded that these discrepancies were due to the surface roughness properties, the terrain heterogeneity, variations in  $T_s$  acquired at the different spatial resolutions,  $\alpha$ ,  $\epsilon_0$ , land use characteristics, and to the non-linear behavior of atmospheric stability. The main novelty of the present study compared with the previously described is that a wider range of resolutions is covered, including very high

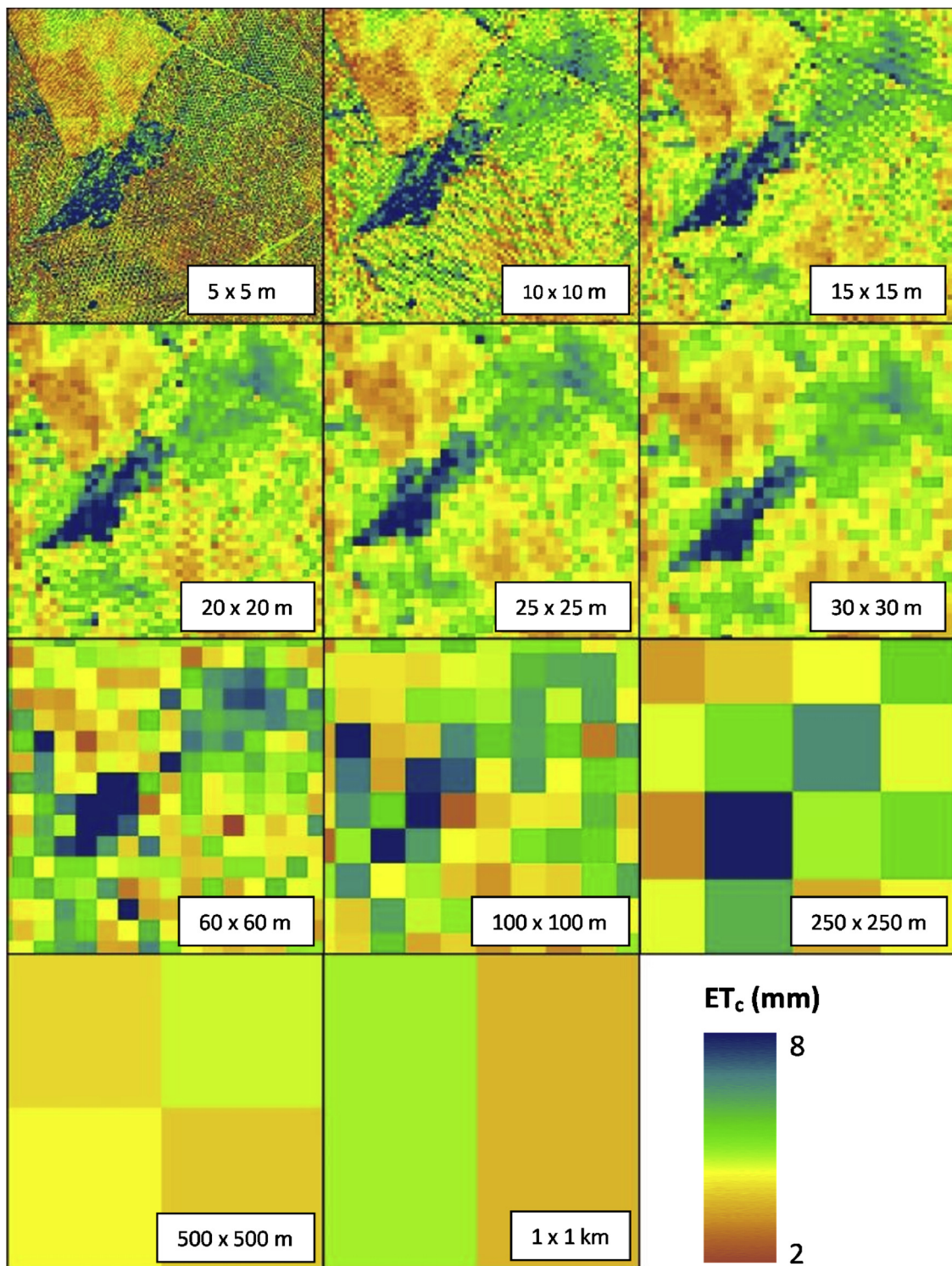


Fig. 9. ET<sub>c</sub> images derived from METRIC for DOY 188 at different spatial resolutions.

resolutions which are acquiring great importance in precision agriculture studies.

Evaluating LE, ET<sub>c</sub> and K<sub>co</sub> reflect that water stress increased from the first to the last date, caused mainly by crop characteristics and crop management (as the stomatal closure or the irrigation amount, among others). Thus, this trend was observed in most of the olive orchards (even those under irrigation as severe deficit irrigation strategies are carried out in the area). This fact, together with the lack of precipitation during the analyzed period, generated decreases in the soil water

content, limiting the plant transpiration (Allen et al., 1998). Regarding the scale effect, an average relative difference of 9% was obtained in this study for ET<sub>c</sub> when using different resolution scales, reaching a maximum discrepancy of 23% (at 1000 × 1000 m pixel size). However, these relative differences follow a pattern in function of the scale. At high resolutions (< 30 × 30 m) the average error found was of around 1–3%, whereas for low resolutions (> 30 × 30 m) this mean error reach 23%. Several studies have analyzed the spatial resolution effect on ET<sub>c</sub> assessment (Su et al., 1999; Sridhar et al., 2003; McCabe and

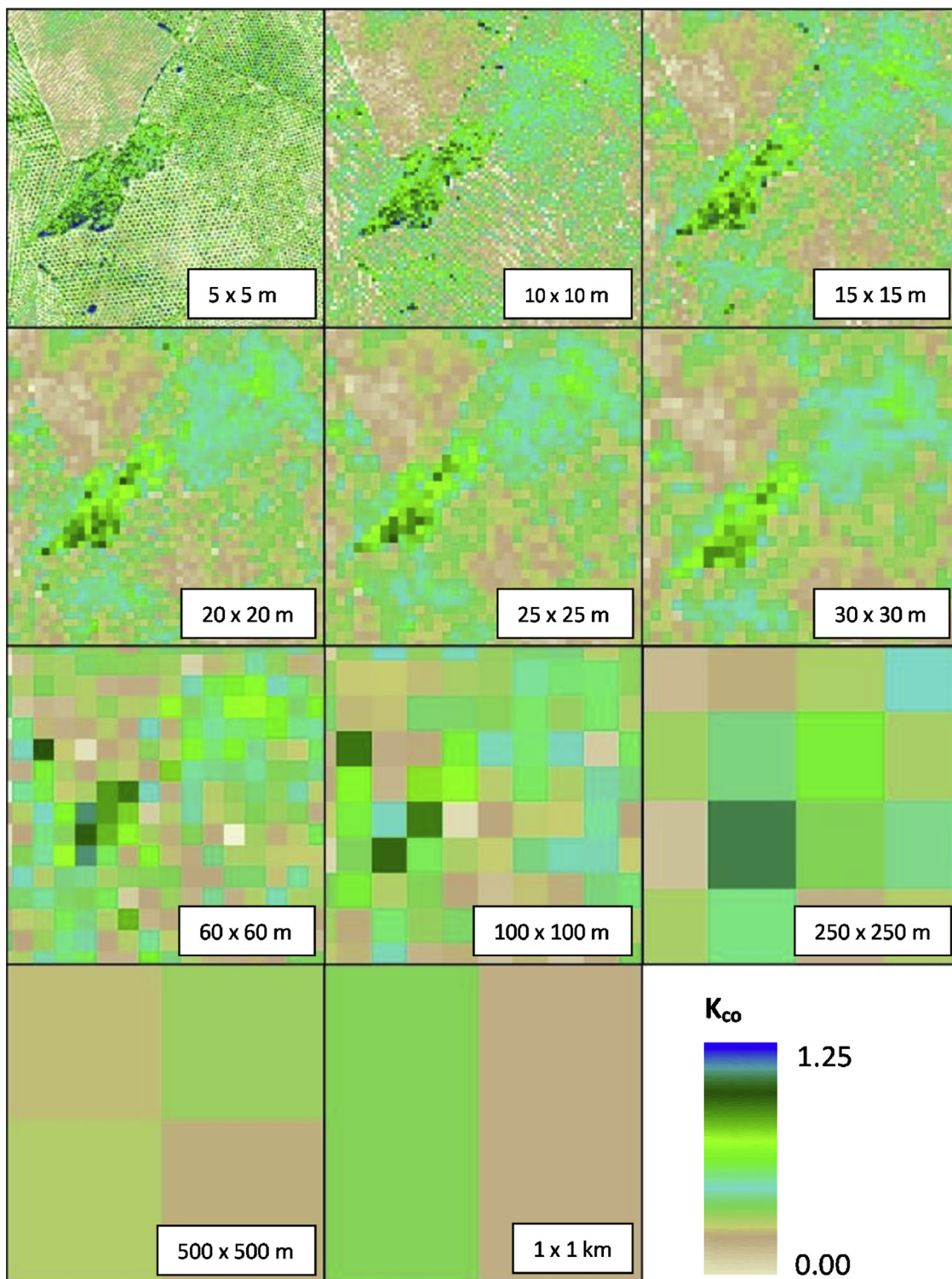


Fig. 10.  $K_{co}$  images derived from METRIC for DOY 188 at different spatial resolutions.

Wood, 2006; Hong et al., 2009; Gebremichael et al., 2010; Tian et al., 2012; Ershadi et al., 2013; Sharma et al., 2016 and Gaur et al., 2017) obtaining also large discrepancies when pixel sizes higher than 30 m were considered. These authors confirm the results obtained in this study, pointing out surface heterogeneity and roughness length parameters as the main causes of these differences.

The evaluation of the four SEB components, and mainly the LE term, indicates that METRIC works well when using high resolution images with heterogeneous agricultural systems such as olive orchards, being

the first study carrying out this analysis. However, significant discrepancies are found when coarse resolution images (higher than  $30 \times 30$  m) are used, caused by the aggregation of non-linear components and by the inclusion of non-agricultural areas in such aggregation when coarse spatial resolutions are considered.

This study has been able to quantify the water requirements of the crops considering different platforms and sensors. Thus, based on these results, irrigation requirements using data from satellites such as MODIS (spatial resolution equal to  $1000 \times 1000$  m) could generate

differences until 23% compared with the use of Landsat satellites. However, the higher temporal resolution of these satellites could counterbalance these differences, allowing a more continuous monitoring of crop water status.

However, this study presents certain limitation that must be addressed in future works. Although METRIC model has been widely validated in homogeneous crop, only a few of them have been focused on discontinuous orchards. Nevertheless, its application over heterogeneous crops presents some uncertainties. Future efforts should be intended for a better understanding of SEB components behavior on these non-homogeneous environments, paying special attention to the accurate determination of aerodynamic resistance characterized by canopy architecture.

## 5. Conclusions

This study assesses the impact of spatial resolution on SEB components estimations by using METRIC model in a heterogeneous olive orchards area. The major key-points derived from this work can be summarized as in the follows:

- Both  $R_n$  and  $G$  estimations showed a near scale-insensitive behavior, with discrepancies of less than 6% for all the resolutions considered, as  $\epsilon_0$  and  $\alpha$  are not severely affected by changes in pixel size.
- $H$  and  $LE$  showed different results in function of the images scale. Thus, for resolutions lower than  $30 \times 30$  m, no great differences were observed in  $H$  and  $LE$  (less than 2%) whereas more pronounced discrepancies (up to 24% for  $H$ , and 15% for  $LE$ ) were found at coarser spatial resolutions.
- Results found in this study reveal that  $\alpha$ ,  $LAI$  and  $\epsilon_0$  were not the reason of such discrepancies, since these parameters showed a small variation due to spatial resolution changes.
- Surface roughness parameters and land use characteristics could be the main two possible sources of these differences but more studies are needed to contrast this hypothesis.

As summary, results presented here illustrate the good performance of METRIC model when using very high-resolution imagery, whereas major errors are found when lower spatial resolution images are used. The use of very high-resolution images provides more detailed spatially distributed  $ET_c$  estimates, allowing a more optimal field management and advise through the identification of areas inside the plot with different characteristics.

## Acknowledgments

This study has been financially supported by the projects RTA2011-00015-00-00 and RTA2014-00030-00-00 funded by the National Institute for Agricultural and Food Research and Technology (INIA) and FEDER 2014-2020 “Programa Operativo de Crecimiento Inteligente”.

## References

- Allen, R.G., Pereira, L.S., Raes, D., Smith, M., 1998. In: FAO (Ed.), *Crop Evapotranspiration: Guidelines for Computing Crop Water Requirements*. FAO Irrigation and Drainage Paper No 56, FAO Irrigation and Drainage Paper. Roma.
- Allen, R.G., Bastiaanssen, W., Tasumi, M., Morse, A., 2001. Evapotranspiration on the watershed scale using the SEBAL model and landsat images. *Proc., 2001 ASAE Annual Int. Meeting, ASAE, St. Joseph, Mich.*, Paper No. 01-2224.
- Allen, R.G., Tasumi, M., Trezza, R., 2007a. Satellite-based energy balance for mapping evapotranspiration with internalized calibration (METRIC) - model. *J. Irrig. Drain. Eng.* 133, 380–394.
- Allen, R.G., Tasumi, M., Morse, A., Trezza, R., Wright, J.L., Bastiaanssen, W., Kramber, W., Lorite, I., Robison, C.W., 2007b. Satellite-based energy balance for mapping evapotranspiration with internalized calibration (METRIC) - applications. *J. Irrig. Drain. Eng.* 133, 395–406.
- Allen, R.G., Pereira, L.S., Howell, T.A., Jensen, M.E., 2011. Evapotranspiration information reporting: I. Factors governing measurement accuracy. *Agric. Water Manag.* 98, 899–920.
- Allen, R.G., Trezza, R., Tasumi, M., Kjaersgaard, J., 2012. METRIC Mapping Evapotranspiration at High Resolution. Applications Manual for Landsat Satellite Imagery. Version 2.0.8. University of Idaho, Kimberly, Idaho.
- Anderson, M.C., Kustas, W.P., Norman, J.M., 2003. Upscaling and downscaling – a regional view of the Soil-Plant-Atmosphere continuum. *Agron. J.* 95, 1408–1423.
- Bastiaanssen, W.G.M., 1995. Regionalization of Surface Flux Densities and Moisture Indicators in Composite Terrain. Dissertation Submitted in Partial Fulfillment of the Requirements for the Degree of Doctor of Philosophy in Agricultural Engineering. Wageningen Agricultural University, Wageningen, Netherlands.
- Bastiaanssen, W.G.M., Menenti, M., Feddes, R.A., Holtslag, A.A.M., 1998a. A remote sensing surface energy balance algorithm for land (SEBAL). 1. Formulation. *J. Hydrol.* 212–213, 198–212.
- Bastiaanssen, W.G.M., Pelgrum, H., Wang, J., Ma, Y., Moreno, J.F., Roerink, G.J., van der Wal, T., 1998b. A remote sensing surface energy balance algorithm for land (SEBAL). 2. Validation. *J. Hydrol.* 212–213, 213–229.
- Berni, J.A.J., Zarco-Tejada, P.J., Sepulcre-Cantó, G., Fereres, E., Villalobos, F., 2009a. Mapping canopy conductance and CWSI in olive orchards using high resolution thermal remote sensing imagery. *Remote Sens. Environ.* 113, 2380–2388.
- Berni, J.A.J., Zarco-Tejada, P.J., Suárez, L., Fereres, E., 2009b. Thermal and narrowband multispectral remote sensing for vegetation monitoring from an unmanned aerial vehicle. *IEEE Trans. Geosci. Remote Sens.* 47, 722–738.
- Bisquet, M., Sánchez, J.M., López-Urrea, R., Caselles, V., 2016. Estimating high resolution evapotranspiration from disaggregated thermal images. *Remote Sens. Environ.* 187, 423–433.
- Brunsell, N.A., 2011. Characterizing the multi-scale spatial structure of remotely sensed evapotranspiration with information theory. *Biogeosciences* 8, 2269–2280.
- Brunsell, N.A., Gillies, R.R., 2003. Scale issues in land-atmosphere interactions: implications for remote sensing of the surface energy balance. *Agric. For. Meteorol.* 117, 203–221.
- Brutsaert, W.H., 1982. *Evaporation into the Atmosphere*. D. Reidel, Boston.
- Bugmann, H., Linder, M., Lasch, P., Flechsig, M., Ebert, B., Cramer, W., 2000. Scaling issues in forest succession modeling. *Clim. Change* 44, 265–289.
- De la Fuente-Sáiz, D., Ortega-Farías, S., Fonseca, D., Ortega-Salazar, S., Kilic, A., Allen, R.G., 2017. Calibration of METRIC model to estimate energy balance over a drip-irrigated apple orchard. *Remote Sens.* 9, 1–18.
- Duke, C., Guérif, M., 1998. Crop reflectance estimate errors from the SAIL model due to spatial and temporal variability of canopy and soil characteristics. *Remote Sens. Environ.* 66, 286–297.
- Ershadi, A., McCabe, M.F., Evans, J.P., Walker, J.P., 2013. Effects of spatial aggregation on the multi-scale estimation of evapotranspiration. *Remote Sens. Environ.* 131, 51–62.
- Famiglietti, J.S., Wood, E.F., 1994. Multiscale modelling of spatially variable water and energy balance processes. *Water Resour. Res.* 30, 3061–3078.
- Gaur, N., Mohanty, B.P., Kefauver, S.C., 2017. Effect of observation scale on remote sensing based estimates of evapotranspiration in a semi-arid row cropped orchard environment. *Precis. Agric.* 18, 762–778.
- Gebremichael, M., Wang, J., Sammis, T.W., 2010. Dependence of remote sensing evapotranspiration algorithm on spatial resolution. *Atmos. Res.* 96, 489–495.
- Giorgi, F., 1997. An Approach for the Representation of Surface Heterogeneity in Land Surface Models. Part I: Theoretical Framework, vol. 125. American Meteorological Society, pp. 1885–1899.
- Gueymard, C.A., 1995. SMARTS, A Simple Model of the Atmospheric Radiative Transfer of Sunshine: Algorithms and Performance Assessment. Technical Report No. FSEC-PR-270-95. Florida Solar Energy Center, Cocoa, FL.
- Harvey, L.D.D., 2000. Upscaling in global change research. *Clim. Change* 44, 225–263.
- Hong, S.-H., Hendrickx, J.M.H., Borchers, B., 2009. Up-scaling of SEBAL derived evapotranspiration maps from Landsat (30 m) to MODIS (250 m) scale. *J. Hydrol.* 370, 122–138.
- Huete, A.R., 1988. A soil-adjusted vegetation index (SAVI). *Remote Sens. Environ.* 25, 295–309.
- Idso, S.B., Jackson, R.D., Reginato, R.J., 1975a. Estimating evaporation: a technique adaptable to remote sensing. *Science* 189, 991–992.
- Idso, S.B., Jackson, R.D., Reginato, R.J., Kimball, B.A., Nakayama, F.S., 1975b. The dependence of bare soil albedo on soil water content. *J. Appl. Meteorol.* 14, 109–113.
- Kool, D., Agam, N., Lazarovitch, N., Heitman, J.L., Sauer, T.J., Ben-Gal, A., 2014. A review of approaches for evapotranspiration partitioning. *Agric. For. Meteorol.* 184, 56–70.
- Kusnierek, K., Korsath, A., 2014. Challenges in using an analog uncooled microbolometer thermal camera to measure crop temperature. *Int. J. Agric. Biol. Eng.* 7, 60–74.
- Kustas, W.P., Li, F., Jackson, T.J., Prueger, J.H., MacPherson, J.I., Wolde, M., 2004. Effects of remote sensing pixel resolution on modeled energy flux variability of croplands in Iowa. *Remote Sens. Environ.* 92, 535–547.
- Leinonen, I., Grant, O.M., Tagliavia, C.P.P., Chaves, M.M., Jones, H.G., 2006. Estimating stomatal conductance with thermal imagery. *Plant Cell Environ.* 29, 1508–1518.
- Liang, S., 2000. Numerical experiments on the spatial scaling of land surface albedo and leaf area index. *Remote Sens. Rev.* 19, 225–242.
- Liu, S., Roujean, J.L., Tchuente, A.T.K., Ceamanos, X., Calvet, J.C., 2014. A parameterization of SEVIRI and MODIS daily surface albedo with soil moisture: calibration and validation over southwestern France. *Remote Sens. Environ.* 144, 137–151.
- Lobell, D.B., Asner, G.P., 2002. Moisture effects on soil reflectance. *Soil Sci. Soc. Am. J.* 66, 722–727.
- Long, D., Singh, V.P., Li, Z.L., 2011. How sensitive is SEBAL to changes in input variables, domain size and satellite sensor? *J. Geophys. Res.* 116, D21107.
- Lorite, I.J., Mateos, L., Fereres, E., 2005. Impact of spatial and temporal aggregation of input parameters on the assessment of irrigation scheme performance. *J. Hydrol.* 300,

- 286–299.
- Lovarelli, D., Bacenetti, J., Fiala, M., 2016. Water footprint of crop productions: a review. *Sci. Total Environ.* 548–549, 236–251.
- McCabe, M.F., Wood, E.F., 2006. Scale influences on the remote estimation of evapotranspiration using multiple satellite sensors. *Remote Sens. Environ.* 105, 271–285.
- Moran, M.S., Jackson, R.D., Raymond, L.H., Gay, L.W., Slater, P.N., 1989. Mapping surface energy balance components by combining Landsat thematic mapper and ground-based meteorological data. *Remote Sens. Environ.* 30, 77–87.
- Moran, S., Humes, S., Pinter Jr., P.J., 1997. The scaling characteristics of remotely-sensed variables for sparsely-vegetated heterogeneous landscapes. *J. Hydrol.* 190, 337–362.
- Norman, J.M., Kustas, W.P., Humes, K.S., 1995. Source approach for estimating soil and vegetation energy fluxes in observations directional radiometric surface temperature. *Agric. For. Meteorol.* 77, 263–293.
- Ortega-Farías, S., Ortega-Salazar, S., Poblete, T., Kilic, A., Allen, R.G., Poblete-Echeverría, C., Ahumada-Orellana, L., Zuñiga, M., Sepúlveda, D., 2016. Estimation of energy balance components over a drip-irrigated olive orchard using thermal and multi-spectral cameras placed on a helicopter-based unmanned aerial vehicle (UAV). *Remote Sens.* 8, 1–18.
- Ortega-Farías, S., Ortega-Salazar, S., Poblete, T., Poblete-Echeverría, C., Zuñiga, M., Sepúlveda-Reyes, D., Kilic, A., Allen, R.G., 2017. Estimation of olive evapotranspiration using multispectral and thermal sensors placed aboard an unmanned aerial vehicle. *Acta Hortic.* 1150, 1–8.
- Paço, T.A., Pôças, I., Cunha, M., Silvestre, J.C., Santos, F.L., Paredes, P., Pereira, L.S., 2014. Evapotranspiration and crop coefficients for a super intensive olive orchard. An application of SIMDualKc and METRIC models using ground and satellite observations. *J. Hydrol.* 519, 2067–2080.
- Pereira, L.S., Oweis, T., Zairi, A., 2002. Irrigation management under water scarcity. *Agric. Water Manag.* 57, 175–206.
- Ramírez-Cuesta, J.M., Kilic, A., Allen, R., Santos, C., Lorite, I.J., 2017. Evaluating the impact of adjusting surface temperature derived from Landsat 7 ETM+ in crop evapotranspiration assessment using high-resolution airborne data. *Int. J. Remote Sens.* 38, 4177–4205.
- Rana, G., Katerji, N., 2000. Measurement and estimation of actual evapotranspiration in the field under Mediterranean climate: a review. *Eur. J. Agron.* 13, 125–153.
- Roerink, G.J., Su, Z., Menenti, M., 2000. SSEBI: a simple remote sensing algorithm to estimate the surface energy balance. *Phys. Chem. Earth Part B Hydrol. Ocean. Atmos.* 25, 147–157.
- Rosa, R.D., Paredes, P., Rodrigues, G.C., Alves, I., Fernando, R.M., Pereira, L.S., Allen, R.G., 2012. Implementing the dual crop coefficient approach in interactive software. 1. Background and computational strategy. *Agric. Water Manag.* 103, 8–24.
- Roxy, M.S., Sumithranand, V.B., Renuka, G., 2010. Variability of soil moisture and its relationship with surface albedo and soil thermal diffusivity at Astronomical Observatory, Thiruvananthapuram, south Kerala. *J. Earth Syst. Sci.* 119, 507–517.
- Santos, C., Lorite, I.J., Tasumi, M., Allen, R.G., Fereres, E., 2008. Integrating satellite-based evapotranspiration with simulation models for irrigation management at the scheme level. *Irrig. Sci.* 26, 277–288.
- Santos, C., Lorite, I.J., Allen, R.G., Tasumi, M., 2012. Aerodynamic parameterization of the satellite-based energy balance (METRIC) model for ET estimation in rainfed olive orchards of Andalusia, Spain. *Water Resour. Manag.* 26, 3267–3283.
- Schulze, R., 2000. Transcending scales of space and time in impact studies of climate and climate change on agrohydrological responses. *Agric. Ecosyst. Environ.* 82, 185–212.
- Senay, G.B., Bohms, S., Singh, R.K., Gowda, P.H., Velpuri, N.M., Alemu, H., Verdin, J.P., 2013. Operational evapotranspiration mapping using remote sensing and weather datasets: a new parameterization for the SSEB approach. *J. Am. Water Resour. Assoc.* 49, 577–591.
- Sharma, V., Kilic, A., Irmak, S., 2016. Impact of scale/resolution on evapotranspiration from Landsat and MODIS images. *Water Resour. Res.* 52, 1800–1819.
- Sridhar, V., Elliott, R.L., Chen, F., 2003. Scaling effects on modeled surface energy-balance components using the NOAA-OSU land surface model. *J. Hydrol.* 280, 105–123.
- Su, Z., 2002. The surface energy balance system (SEBS) for estimation of turbulent heat fluxes. *Hydrol. Earth Syst. Sci.* 6, 85–99.
- Su, Z., Pelgrum, H., Menenti, M., 1999. Aggregation effects of surface heterogeneity in land surface processes. *Hydrol. Earth Syst. Sci.* 3, 549–563.
- Sugathan, N., Biju, V., Renuka, G., 2014. Influence of soil moisture content on surface albedo and soil thermal parameters at a tropical station. *J. Earth Syst. Sci.* 125, 1115–1128.
- Tang, R., Li, Z.-L., Chen, K.-S., Jia, Y., Li, C., Sun, X., 2013. Spatial-scale effect on the SEBAL model for evapotranspiration estimation using remote sensing data. *Agric. For. Meteorol.* 174–175, 28–42.
- Tasumi, M., Allen, R.G., Trezza, R., Wright, J.L., 2003. Soil heat flux estimation method. Appendix 12. In: Tasumi, M. (Ed.), *Progress in Operational Estimation of Regional Evapotranspiration Using Satellite Imagery*. PhD Diss. University of Idaho, Moscow, ID.
- Tasumi, M., Allen, R.G., Trezza, R., 2008. At-surface reflectance and albedo from satellite for operational calculation of land surface energy balance. *J. Hydrol. Eng.* 13, 51–63.
- Tian, H., Wen, J., Wang, C.H., Liu, R., Lu, D.R., 2012. Effect of pixel scale on evapotranspiration estimation by remote sensing over oasis areas in north-western China. *Environ. Earth Sci.* 67, 2301–2313.
- Wallender, W.W., Grismer, M.E., 2002. Irrigation hydrology: crossing scales. *J. Irrig. Drain. Eng.* 128, 203–211.
- Weidong, L., Baret, F., Xingfa, G., Qingxi, T., Lanfen, Z., Bing, Z., 2002. Relating soil surface moisture to reflectance. *Remote Sens. Environ.* 81, 238–246.
- Winter, J.M., Lopez, J.R., Ruane, A.C., Young, C.A., Scanlon, B.R., Rosenzweig, C., 2017. Representing water scarcity in future agricultural assessments. *Anthropocene* 18, 15–26.
- Yang, G., Pu, R., Zhao, C., Xue, X., 2014. Estimating high spatiotemporal resolution evapotranspiration over a winter wheat field using an IKONOS image based complementary relationship and lysimeter observations. *Agric. Water Manag.* 133, 34–43.
- Zia, S., Spohrer, K., Du, W., Spreer, W., He, X., Muller, J., 2010. Effect of wind and radiation on the crop Water stress index derived by infrared thermography. *Conference on International Research on Food Security* 3–6.
- Zipper, S.C., Loheide II, S.P., 2014. Using evapotranspiration to assess drought sensitivity on a subfield scale with HRMET, a High Resolution Surface Energy Balance Model. *Agric. For. Meteorol.* 197, 91–102.